Effect of Ag addition on the thermal characteristics and structural evolution of Ag-Cu-Ni ternary alloy nanoclusters: Atomistic simulation study

Ram Subbaraman[1] and Subramanian K. R. S. Sankaranarayanan[2,*]

[1]*Nuclear Engineering Department, Argonne National Laboratory, Argonne, Illinois 60439, USA*
[2]*Center for Nanoscale Materials, Argonne National Laboratory, Argonne, Illinois 60439, USA*

Atomic-scale compositional variation in Ag contents across Ag-Cu-Ni alloy upon being subjected to repeated annealing cycles is shown to result in significant differences in the structure and the thermal stability of ternary alloy nanoclusters. Molecular dynamics (MD) simulations employing quantum Sutton–Chen potentials were used to investigate the effect of Ag addition on the thermal characteristics of Ag-Cu-Ni ternary alloy nanoclusters of 4-nm diameter. The initial configurations were generated using Monte Carlo simulations and comprise surface-segregated structures with the lowest surface energy component, Ag, occupying low coordination sites such as corners, edges, and faces. A compositional oscillation between the Cu and Ni atoms was observed for layers beneath the surface which transitions into a bulk alloy composition at the core. We find that the Cu-Ni binary alloys on being subjected to annealing schedules demonstrated an increase in thermal stability, as indicated by the increase in melting points. The annealed configurations of the Ag-Cu-Ni ternary alloy, on the other hand, showed a nonmonotonic behavior. For Ag compositions less than 20%, we observe an initial increase in melting point followed by a decrease in the third cycle. For higher Ag compositions (>20%), we observe a decrease in melting point with annealing; the rate of decrease is strongly correlated to the Ag composition in the alloy. Cu-Ni nanoclusters having 50% Cu showed a transition from an initial icosahedral to a cuboctahedron-like structure whereas Ag-rich Ag-Cu-Ni ternary alloys showed a transition from icosahedral to an amorphous structure. Compositional analysis based on radial distribution functions and density profiles indicate that these transitions were dependent on the distribution of the alloying elements in the nanocluster. Calculated root-mean-square displacements and diffusion coefficients indicate that the rate of mixing of Ag increases with Ag content in the Ag-Cu-Ni ternary alloy. Ternary alloys show heterogeneous melting during the first heating cycle followed by a bulk-like melting during the subsequent annealing cycles. The simulation results are consistent with available experimental studies.

I. INTRODUCTION

The possibility of controlling the atomic-scale structure and tuning of the chemical composition of particles at the nanoscale level is of enormous importance for both basic science and technological applications.[1,2] In particular, the ability to tailor the size and composition of metal particles at the nanoscale levels could lead to improved or altered functional properties.[3–5] For example, the exploratory efforts involving nanotechnology-guided design and fabrication of binary or ternary alloy nanoparticles have primarily focused on enhancing the catalytic activity and selectivity and reducing the cost of catalysts.[6,7] The characterization of the atomic-scale distribution on the nanoalloy surface as a function of overall composition, shape, and size and synthesis conditions is an essential step in materials design for catalysts in emerging energy technologies.[8,9] Additionally, the cost, availability, and recyclability of precious transition metals such as Pt, Ru, Au, and Ag used for catalysis in various emerging energy technologies have been identified as a significant bottleneck toward successful deployment of electrochemical energy storage or conversion devices.[10] One of the means of circumventing this issue is the use of alloy materials.[11] Binary and ternary alloys of a catalytically active metal with less-expensive stable metals has been identified as a viable option with some alloy materials demonstrating activities better than the pristine catalytic materials themselves.[12] The surface segregation, mixing properties, and thermodynamic

phase diagrams of alloys, while well understood for bulk systems, are seldom very clearly defined for nanostructures.[13] Improved surface–volume ratios associated with nanocatalysts make them a very attractive candidate for energy and catalytic applications.[6] Understanding the dynamics of formation, evolution of morphology, and surface features in the case of multimetallic systems is still an active area of research.[3–5,8,14]

While single-component metal clusters have been extensively investigated,[15,16] much less attention has been devoted to the study of bimetallic and trimetallic nanoclusters.[17–19] Binary and ternary alloys of metals such as Cu, Ni, and Ag find applications in emerging energy technologies, heterogeneous catalysis, microelectronics, sensing, optoelectronic, magnetic, and even medical applications.[13] For example, Ag-Cu alloy nanoparticles have been shown to be promising candidates as lead-free interconnects.[20] Also, the Ag-Cu alloy has been recently proposed as a catalyst with improved selectivity for ethylene epoxidation, compared with pure silver.[21] The Ag-Cu nanoalloy has also shown significantly improved optical properties, as demonstrated in recent fluorescence quenching studies by Chowdhury *et al.*[22] Similarly, Cu-Ni alloy nanoclusters have displayed interesting magnetic properties, whereas Ag-Ni alloys have been utilized as shape-memory alloys for medical applications.[23,24]

These studies have clearly demonstrated that the functional properties can be dramatically altered by alloying two elements. It is therefore expected that the ternary alloy properties

would be significantly different from those of the constituent elements as well as their binary alloys. While the energetic descriptions are reasonably defined for binary alloys,[25,26] ternary systems, due to the dearth of information regarding the cross-correlation behavior of various alloy elements, create an even more complex scenario for characterization and understanding of the properties.[13] There are several factors which play a critical role in determining the final atomic distribution in binary and ternary nanoalloys. These include miscibility of the constituent atoms (characterized by their heats of solution), the surface energies, the lattice mismatch, and the electronegativities of constituent elements. In addition to the interatomic interactions, the properties of multicomponent systems are significantly influenced by relative concentrations.[13] Additional complexity in these systems results from the surface segregation phenomenon and micromixing at the surface.[27] There is thus very little quantitative data on the structure and energetics of bulk and surface regions governing the properties of ternary alloy nanostructures, and a comprehensive understanding of the same is needed.[13] Computer simulations offer an effective tool to study properties of nanoclusters and complement ongoing experimental efforts.[18–30]

Considerable experimental and theoretical research has been dedicated to understanding the thermodynamics and kinetics of single metal and binary alloy nanoparticle growth and stabilization when subjected to thermal and other stresses.[13,17,31,32] The final atomic arrangements in alloy nanoclusters have been found to be strongly influenced by thermodynamic factors and growth kinetics.[32] In particular, molecular dynamics has also been used to investigate the thermal and structural properties of bimetallic nanoparticles including the effects of size, composition, and structure on the melting and thermodynamic properties.[18,27–29,33,34] The systems that have been extensively studied include Ag-Pd, Au-Pd, Cu-Ni, Pd-Pt, Au-Pt, Ag-Ni, and Ag-Co, to name a few. The melting of binary metallic nanoclusters of Ag-Ni and Ag-Co was studied at 'magic' sizes for the anti-Mackay icosahedron by Kuntova *et al.*[35] They find that the core-shell structure is especially stable for compositions at which the external shell is completely made of silver, while the inner core is either made of Ni or Co. Oviedo *et al.*[36] studied the formation of binary core-shell nanoparticles composed of Au, Ag, and Pt atoms and found that, depending on the particle size and core structure, as well as on the under/over-saturation conditions applied, it was possible to obtain different degrees of decoration of the core nanostructure.[36] Similarly, Xiao *et al.* have investigated the size effect on alloying ability and phase stability of immiscible bimetallic nanoparticles.[37] Mejía-Rosales *et al.* have used molecular dynamics simulations to investigate the features of specific atomic sites at the surface, which can be related to the high catalytic activity properties of the particles.[38]

Although several other such examples of bimetallic nanoparticles exist in literature,[13,17,18,25,26,39–41] there have been very limited studies on investigating the melting and thermodynamic properties of ternary alloy nanoclusters. In particular, the effect of systematic addition of the third component on the melting characteristics and structural evolution of binary alloy nanoclusters has not been investigated. In this paper, we explore the melting and recrystallization behavior

of ternary alloy nanoclusters of Ag, Cu, and Ni in the 2-4 nm diameter size range. First, we investigate binary alloys of Ag, Cu and Ni, i.e., Ag-Cu, Cu-Ni, and Ni-Ag of equimolar compositions. Then, utilizing Cu-Ni alloy as a representative case, we investigate the role of the third alloying element, i.e. Ag, on the thermodynamic properties and structural features of the ternary Ag-Ni-Cu alloy nanoclusters upon being subjected to three successive heating-cooling schedules. Our aim is to investigate the effect of the atomic-level structural and compositional variations on the thermodynamics and melting characteristics of Ag-Cu-Ni trimetallic nanoclusters via selective and incremental addition of Ag (10%–50%) to the Cu-Ni alloy.

II. INITIAL CONFIGURATION SETUP

A. Nanocluster size and shape

Shape-controlled synthesis of nanoparticles has paved way toward understanding properties of nanoparticles, physical, thermal, and catalytic, in great detail.[42,43] Icosahedron, a platonic solid, offers unique properties due to the presence of (111)-type symmetry for the surface atoms. Controlling the "surface orientation" for a nanoparticle plays a crucial role in designing and synthesizing nanoparticles for various applications, particularly catalysis, where surface orientation can offer unique mode of tailoring material properties.[13] In this paper, we have mainly focused on icosahedral particle geometries for our alloy nanoparticles. As we establish through the following sections, the relative stability of the structure is a function of the components' composition as well as thermal history along with the composition of the destabilizing–stabilizing element in the alloy. A 10-shell particle (denoted hereafter as 4 nm, the approximate diameter) comprising 3871 atoms was studied. Initial structures were constructed using a lattice spacing calculated based on the compositional average of the individual lattice spacing. To thoroughly evaluate the Monte Carlo (MC) energy code, the initial distribution of the atoms in the particle was the opposite of what is expected based on energetics. For example, for the case of a binary Cu-Ni (50–50) alloy, for which the equilibrium structure is made of copper atoms enriching the outer surface, all the copper atoms were placed in the interior of the particle. For the case of ternary alloys, the silver atoms were placed in the innermost shells, followed by copper and nickel atoms. The equilibrium atom distribution as well as the atom spacing was then evaluated using the MC simulation procedure. The generated structure was then subjected to a MC simulation employing an embedded atom model (EAM) to generate the minimum energy initial configurations, which are used subsequently for studying the melting-recrystallization phenomena.

B. Monte Carlo simulation technique

MC simulations, in combination with the EAM formulation, were used to predict the structure of clusters containing three different kinds of atoms for various cluster compositions. The detailed description of the EAM formalism utilized here

has been documented in Refs. 44–46. The state of the system was characterized by the energy of the system as given by

$$U_{tot} = \sum_i F_i \left(\sum_{j \neq i} \rho_j(r_{ij}) \right) + \frac{1}{2} \sum_i \sum_{j \neq i} \phi_{ij}(r_{ij}). \quad (2.1)$$

In the above equation, ρ_j is the electron density due to atom j. The first term is the embedding energy for atom i which is embedded into the background electron density, and the second term is the core-core pair repulsion between atom i and j separated by a distance R_{ij}. The force field parameters used to model Ag, Cu, and Ni were obtained from the work of Wadley *et al.*,[47] and the parametrization strategy for the alloys is similar to that by described in the work of Johnson.[48]

The standard Metropolis MC method was used to generate the minimum energy configuration at 300 K. MC simulation methods based on the Metropolis algorithm have been successfully used in previous surface-segregation calculations for various alloys to generate equilibrium alloy configurations and provide an average thermodynamic profile over a thermodynamic equilibrium ensemble. The MC simulations were carried out in a canonical ensemble where the total number of atoms of each element and the temperature were held constant. In the MC approach, starting from an initially randomly distributed atomic configuration of the alloy, the successive configurations are generated in proportion to the probabilities of a configuration occurring in the equilibrium ensemble. During each of the MC steps, one of the following two configurational transformations is tried out with an equal probability: (1) We displace a randomly selected atom from its original position in a random direction. The magnitude of the displacement is chosen to be in the range of $(0, r_{max}]$. (2) Two randomly selected atoms with different element types are exchanged and the atoms are switched in the lattice.

The convergence was obtained when the minimum energy obtained during the simulation steps became constant ($\Delta E < 0.01$ eV), and the state of the system corresponding to that minimum energy was retained as shown in Fig. 1. A large number of simulations (100), with random initial configurations, each having (1000 times the total number of atoms) steps, were performed to ensure convergence.

The initial MC simulations focused on investigating the equilibrium microstructures of Ag-Cu, Ag-Ni, and Cu-Ni binary alloys. In all the cases, we find that the lower surface energy component, i.e., Ag in Ag-Cu and Ag-Ni and Cu in Cu-Ni, segregated to the surface whereas the core comprised the higher surface energy component (Cu in Ag-Cu, Ni in Ag-Ni, and Ni in Cu-Ni). The extent of segregation was quantitatively compared with that obtained for various different potential models such as the quantum Sutton–Chen (QSC) and bond order simulation model developed by DePristo and co-workers.[49–51] In all the cases, we find that the segregation profile and the extent of segregation showed an excellent agreement, both qualitatively and quantitatively, validating the choice of potential used in the MC simulations. While very little information is available in the literature regarding the phase segregation properties of ternary alloys, binary alloys are well studied for the three components listed here, namely, Ag, Cu, and Ni. Experimental evidence for Ag segregation in both Ag-Cu and Ag-Ni alloys has been shown
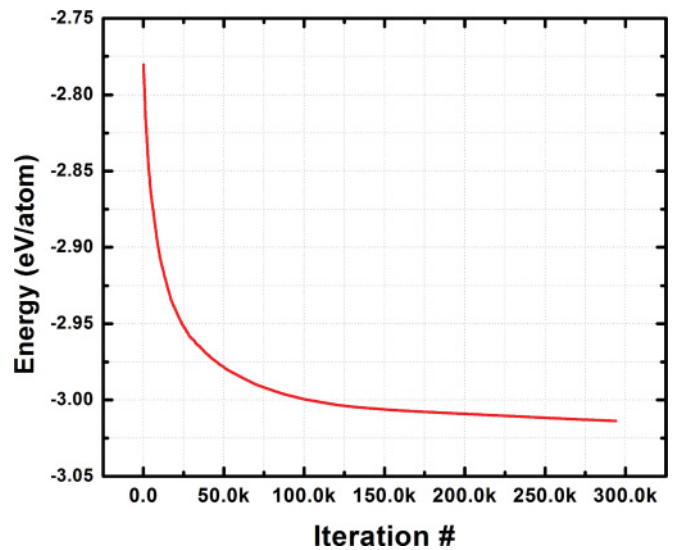

FIG. 1. (Color online) Sample energy variation during MC simulations of binary and ternary alloy nanoclusters as a function of the MC iteration. The system energy converges after ~150 000 iterations for 34%Ag-33%Cu-33%Ni shown here.

for alloy nanoparticle systems.[52,53] Experimental techniques such as x-ray photoemission spectroscopy, low-energy ion scattering, and optical spectroscopy can be used to clearly identify the surface-segregation characteristics. The relatively large size mismatch and immiscibility of Ag and the other metal components are the driving forces for such segregation phenomena. Cu-Ni systems have also been studied via both theoretical[49–51] as well as experimental methods and found to exhibit similar segregation behavior.[54,55] This suggests that, for the ternary alloy systems, the surface-segregation properties will indeed be driven by the relative lattice mismatch as well as enthalpic considerations involving mixing and surface energetics.

The MC simulations for the ternary Ag-Cu-Ni alloy nanoclusters suggest that the energetically favorable configurations comprise surface-segregated structures with the lower surface energy atoms of Ag preferentially occupying low coordination sites such as corners, edges, and surfaces. The surface energies of the constituent elements are in the Ag < Cu < Ni order. For the lower composition of Ag (10%–25%) in the ternary alloy, the surface sites were also populated with Cu atoms whereas the core comprised primarily Ni atoms. When the composition of Ag in the ternary alloy was increased to ~33%–50%, the surface composition of Ag also increased, which resulted in pushing the Cu atoms to the cluster interior. The number of surface atoms for a 4-nm cluster constitutes ~34% of total atoms and at 34% Ag we observe that all the surface atoms are Ag atoms. Figure 2 shows a typical evolution of compositional profile from one such MC simulation. For the case presented, 50%Ag25%Ni25%Cu, there are enough Ag atoms to completely cover the surface. As a result, a segregated profile is observed. For lower Ag compositions, as will be shown later, Cu atoms are observed on the surface due to the lack of sufficient Ag atoms to saturate the surface. An interesting thing to note for higher Ag compositions was that the layer of atoms below the surface
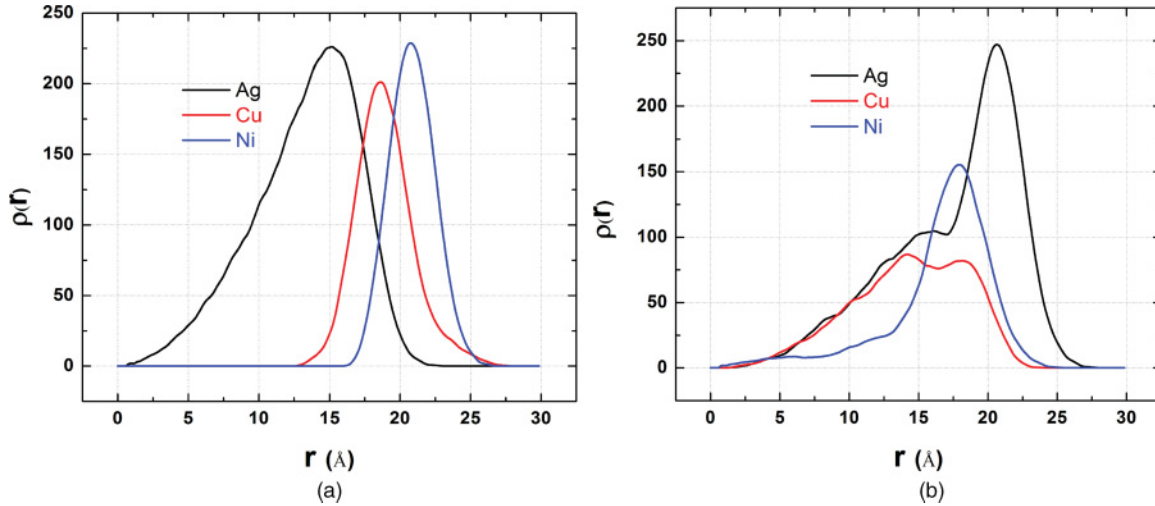
FIG. 2. (Color online) Compositional profile for a $Ag_{0.50}$-$Ni_{0.25}$-$Cu_{0.25}$ ternary alloy nanocluster: (a) initial configuration of the ternary alloy, (b) final equilibrated configuration of the ternary alloy showing the surface segregation of Ag.

was occupied by Ni atoms, which is similar to that observed in other Ni–noble metal alloys (for example Pt_3Ni alloys). Further analysis of the equilibrium composition profile suggests that the composition of Cu and Ni in the first few layers below the surface essentially oscillates till the bulk composition is reached as we approach the cluster core. This behavior has been observed in the case of Ni-Cu-Pd nanoclusters by Polak and Rubinovich *et al.*, where, depending on the temperature and the overall composition, compositional oscillations were observed in Ni-based ternary alloys,[56,57] although, in their case, they observed a compositional oscillation between Cu and Pd atoms, with Cu displacing Pd atoms to the core as its composition was increased. Here, we observe compositional oscillations of Cu and Ni below the cluster skin which can be tuned based on the overall composition of Ag in the ternary alloy system. The final compositional distribution is thus dictated by the competition between energetic and entropic factors. These minimum energy configurations were utilized in the MD simulations to study the structural evolution and melting characteristics of the ternary alloy nanoclusters.

III. COMPUTATIONAL DETAILS

MD simulations using DLPOLY have been used to gain insights into the melting process at the atomistic level for the ternary alloy nanoclusters.[58] Based on the Sutton–Chen potential, the potential energy of the finite system is given by,[59,60]

$$U_{\text{tot}} = \sum_i U_i = \sum_i \varepsilon \left[\sum_{j \neq i} \frac{1}{2} V(r_{ij}) - C\rho i^{1/2} \right]. \quad (3.1)$$

Here, $V(R_{ij})$ is a pair potential to account for the repulsion resulting from Pauli's exclusion principle:

$$V(r_{ij}) = \left(\frac{a}{r_{ij}} \right)^n. \quad (3.2)$$

The local density accounting for cohesion associated with any atom i is given by

$$\rho_i = \sum_{j \neq i} \phi(r_{ij}) = \sum_{j \neq i} \left(\frac{a}{r_{ij}} \right)^m. \quad (3.3)$$

The QSC potential includes quantum corrections and takes into account the zero point energy, allowing better prediction of temperature-dependent properties.[59] The QSC parameters were optimized by Kimura *et al.*[59] from the original Sutton–Chen parameters in order to describe the lattice parameter, cohesive energy, bulk modulus, elastic constants, phonon dispersion, vacancy formation energy, and surface energy. A detailed description of the potential function and its application to predicting viscosity of liquid metal alloys as well as alloy melting and solidification to form a crystal or a glasslike structure is given in Ref. 59. The QSC parameters for the various components are listed in Table I. The geometric mean was used to obtain the energy parameter ε and the arithmetic mean was used for the remaining parameters, to predict the nature of various pairwise interactions.

The QSC potential used in the present study accurately models the thermal properties of transition metals. In several of our previous works[18,27–29] we reported thermal characteristics and melting points of transition metal nanoalloys of Pd, Cu, Rh, and Pt calculated using MD simulations employing the QSC potential function. They agree reasonably well with the experiments reported in the literature.[34,61,62] There are several

TABLE I. Potential parameters used in MD simulations for Ag-Cu-Ni clusters.

Quantum Sutton-Chen	N	M	ε (eV)	C	a (Å)
Ag	11	6	3.945×10^{-3}	96.524	4.0691
Cu	10	5	5.7921×10^{-3}	84.843	3.6030
Ni	10	5	7.3767×10^{-3}	84.745	3.5157

other instances of the application of the QSC potential to characterize nanomaterials in the literature as well.[41,63–66] To validate the observed behavior as being potential independent, additionally we have also performed the simulations using the embedded atom method and obtained qualitatively the same results. All the essential features of this study on the ternary alloy nanocluster were reproducible using the embedded atom method as well. These include the differences in surface-melting characteristics, the composition-dependent crystalline to amorphous transition, and the annealing effect on thermal characteristics. The melting temperatures obtained using the embedded atom method were ±20 K of those predicted using QSC potential parameters.

The MD simulations were carried out in an ensemble approximating the canonical ensemble with a constant number of atoms N and volume V (much larger than the cluster size) without any periodic boundary conditions. A constant-temperature Berendsen thermostat with a relaxation time of 0.4 ps was used for all the simulation runs. The equations of motion were integrated using verlet leapfrog algorithm with

time step of 0.001 ps. The nanocluster was initially subjected to mild annealing in the 0–300 K interval. This was followed by heating to 1600 K in increments of 100 K. Near the melting point, the temperature increments were reduced to 5–10 K to account for the large temperature fluctuations. The simulations were carried out for 400 ps of thermal equilibration followed by production time of 600 ps for generating time-averaged properties.

IV. RESULTS AND DISCUSSION

The transition temperature from a solid to a liquid phase is usually identified by studying the variation in either the thermodynamic properties such as potential energy and specific heat capacity or some structural properties such as bond orientational order parameters. We employ both these methods to identify melting and freezing points for different cluster sizes and alloy compositions as they are subjected to successive heating-cooling cycles.
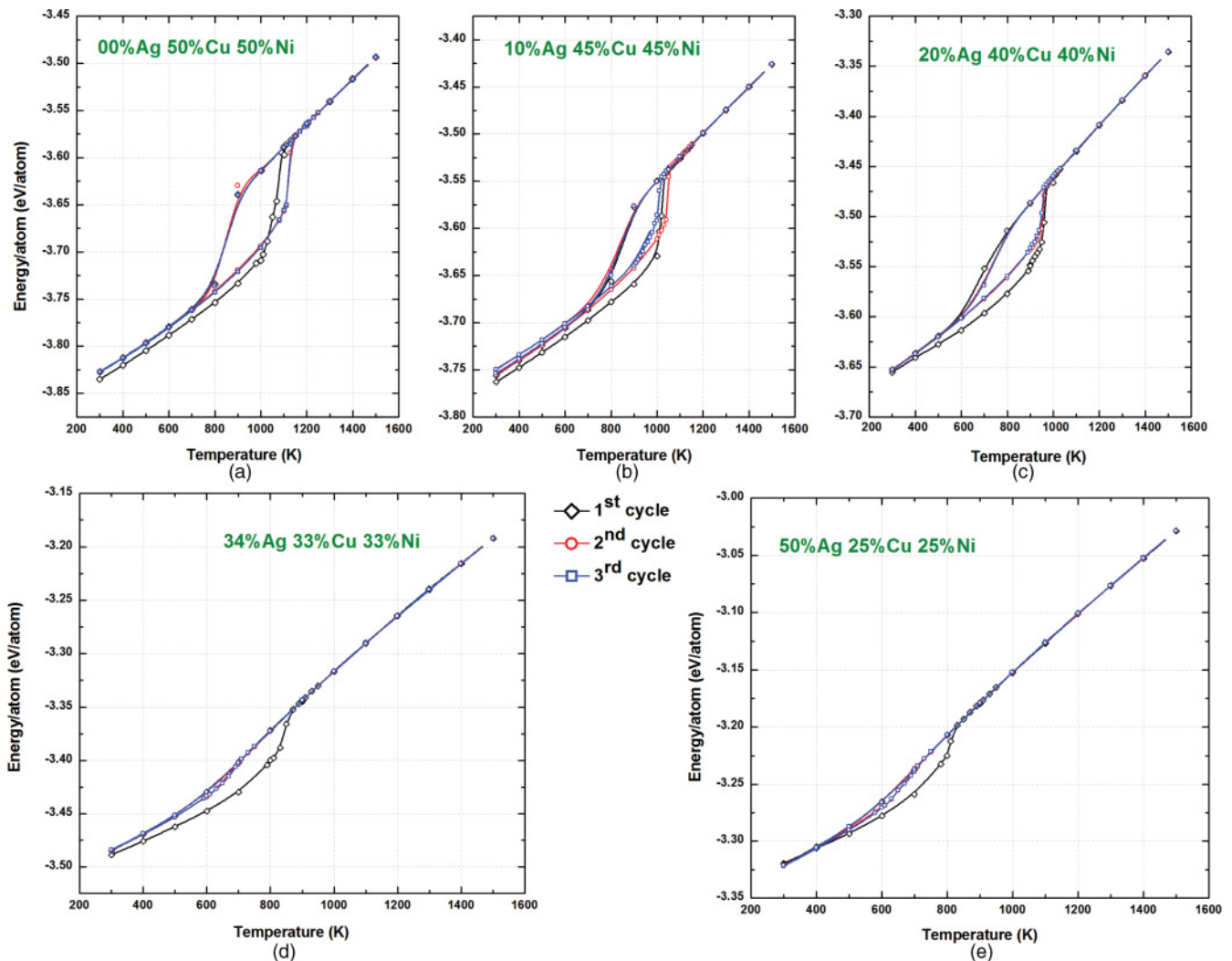

FIG. 3. (Color online) Variations of potential energy with temperature for the various compositions of Ag-Cu-Ni ternary alloy nanoclusters: (a) 0%Ag-50%Cu-50%Ni, (b) 10%Ag-45%Cu-45%Ni, (c) 20%Ag-40%Cu-40%Ni, (d) 34%Ag-33%Cu-33%Ni, (e) 50%Ag-25%Cu-25%Ni. The melting point can be estimated based on the jump in potential energy curve and is shown for a series of three annealing cycles for each of the simulated alloy compositions.

A. Thermodynamic properties

1. Potential energy

Figure 3 shows the temperature dependence of potential energy for various compositions of 4-nm-diameter Ag-Cu-Ni ternary alloy nanoclusters. The transition from a solid to a liquid phase can be identified by a simple jump in the total potential energy curve. This corresponds to a melting point of 1100 K and 850 K for 50%Cu-50%Ni and 34%Ag-33%Cu-33%Ni, respectively, for the first heating cycle. Upon subsequent annealing, the 50%Cu-50%Ni nanocluster shows an increase in melting point to 1130 and 1150 K, respectively, for the second and third annealing cycles. On the other hand, the 50%Ag-25%Cu-25%Ni shows a decrease in melting point to 700 and 680 K, respectively for the second and third annealing cycles.

We have also simulated several intermediate compositions to study the effect of progressively increasing the Ag composition on the melting-point variation for each of the three annealing cycles. Introducing 10% Ag into a Cu-Ni binary alloy resulted in a decrease of melting point for the first annealing cycle to 1020 from 1100 K (for 50%Cu-50%Ni). For the second annealing cycle, this 10%Ag-45%Cu-45%Ni shows an increase in melting point to 1050 K, indicating that the nanocluster thermal stability increases upon annealing. The melting point for the third annealing cycle for this composition, however, shows a decrease to 1000 K, which suggests a decrease in thermal stability. The melting points for the various alloy compositions and for each of the three annealing cycles are shown in Fig. 4.

Upon further increasing of the Ag composition from 10% to 20%, the melting point shows a decrease for each subsequent annealing cycle. The melting point decreases from 960 to 950 to 940 K for the first, second, and third annealing cycles, respectively. Systematic increases in Ag composition to 34% and 50% resulted in similar thermal behavior, except that the rate of decrease in the melting point is higher for the

higher Ag content alloy. For 34% Ag composition, the melting points were 850, 710, and 700 K for the first, second, and third annealing cycles, respectively, whereas for the 50% Ag composition, the melting points were 810, 700, and 690 K, respectively, for the first, second, and third annealing cycles. While the binary alloy nanocluster of Cu-Ni shows increasing thermal stability upon annealing, the addition of Ag to the Cu-Ni alloy seems to induce thermal instability in the ternary alloy nanoclusters. The extent of instability seems to increase as the Ag composition increases beyond 10% Ag in the ternary alloy nanocluster. We would like to point out that on subsequent annealing cycles beyond the third cycle the trends continue, albeit asymptotically, suggesting that the changes are incrementally small.

The potential energy curves also reveal the presence of hysteresis during the melting–freezing cycles. Note that hysteresis is a characteristic of nonbulk or finite-sized systems. As illustrated in the work of Lewis *et al.*, it is easier for clusters to go from an ordered state to a disordered state, i.e., melt rather than the opposite (freeze) during the finite time covered during the simulation.[32] This explains the hysteresis observed between the melting and cooling and indicates the melting temperature to be much closer to the thermodynamic transition point than the freezing temperature. The presence of hysteresis in melting–freezing transition is therefore not unusual and is expected both theoretically[32,67] and experimentally, as reported in the cases of Pb[68] and Na.[69] The structural changes resulting from cooling and melting also influence the phase transition and result in hysteresis, as reported by Chausak and Bartell[70] in their study on freezing of Ni-Al bimetallics. It is important to point out that the hysteresis behavior follows the overall melting characteristic exhibited by the alloys, i.e., as the melting temperatures decrease for the alloys, hysteresis is also found to decrease.

2. Specific Heat Capacity

The specific heat capacity in a weak coupling ensemble such as is achieved with the Berendsen thermostat can be written as a function of fluctuations in the potential energy $\langle \delta(E_p)^2 \rangle$

$$C_v = \frac{k\langle (\delta E_p)^2 \rangle}{(kT)^2 - 2\alpha\langle (\delta E_p)^2 \rangle/3N}, \qquad (4.1)$$

where $\langle (\delta E_p)^2 \rangle = \langle E_p^2 \rangle - \langle E_p \rangle^2$ and α is the ratio of the standard deviations of kinetic and potential energies:

$$\alpha = \sqrt{\langle (\delta KE)^2 \rangle / \langle (\delta E_p)^2 \rangle}. \qquad (4.2)$$

It should be noted that Morishita[71] has proved that a weak coupling ensemble approaches a canonical ensemble for very short relaxation times ($\alpha \approx 0$) and a microcanonical ensemble for longer relaxation times ($\alpha \approx 1$). In the present case, the Berendsen thermostat with a coupling parameter of 0.4 ps leads to $\alpha \approx 10^{-4}$, making the calculations for specific heat capacity similar to that of a canonical ensemble as given by

$$C_v = \frac{k\langle (\delta E_p)^2 \rangle}{(kT)^2}. \qquad (4.3)$$

To identify the melting temperature, the specific heat capacity at constant volume is plotted in Fig. 5. In the case of the
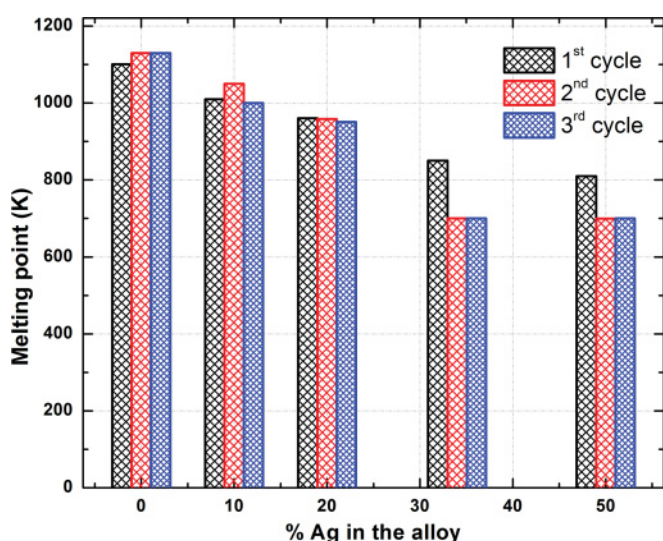
FIG. 4. (Color online) The effect of Ag addition on the melting-point variation in a ternary alloy nanocluster for a series of three annealing cycles. The Ag composition is systematically varied from 0% to 50% Ag in a Ag-Cu-Ni ternary alloy nanocluster.
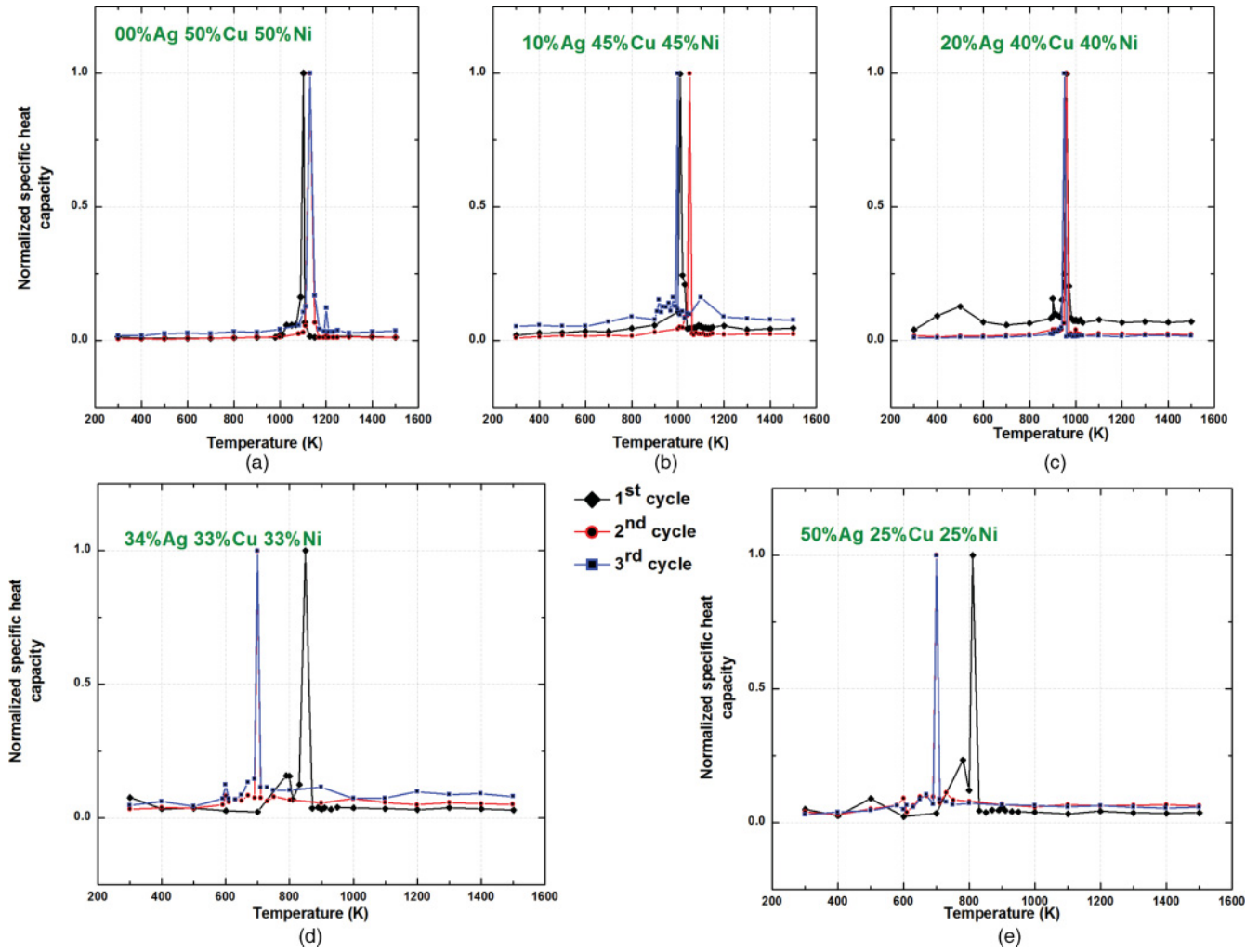
FIG. 5. (Color online) Variations in specific heat capacity with temperature for the various compositions of Ag-Cu-Ni ternary alloy nanoclusters. The Ag composition is systematically varied from 0% to 50% Ag in a Ag-Cu-Ni ternary alloy nanocluster: (a) 0%Ag-50%Cu-50%Ni, (b) 10%Ag-45%Cu-45%Ni, (c) 20%Ag-40%Cu-40%Ni, (d) 34%Ag-33%Cu-33%Ni, (e) 50%Ag-25%Cu-25%Ni. The melting point can be estimated based on the peaks in the specific heat capacity curves and is shown for a series of three annealing cycles for the various alloy compositions.

50%Cu-50%Ni binary alloy cluster, the maximum in the specific heat capacity corresponds to the temperature where a jump in potential energy is observed, i.e., 1100–1110 K. This leads to a melting temperature $T^m = 1100 \pm 10$ K for the first annealing cycle. Similarly, we find that, for the 50%Cu-50%Ni nanocluster, the specific heat capacity calculations show an increase in melting point to 1130 and 1150 K, respectively, for the second and third annealing cycles. As seen from Fig. 5, the variation in the melting points for the other ternary alloy compositions is also consistent with those obtained based on the potential energy curves.

B. Structural variation

1. Bond orientational order parameter

The bond order parameter method can be used to analyze cluster structure as well as to distinguish between atoms in solid (closely packed) and liquid environments[72]. To determine the orientational order, spherical harmonic basis functions

$Y_{lm}(\theta_{ij}, \varphi_{ij})$ are associated with every bond connecting an atom to its near neighbors. Here, Θ and Φ refer to polar and azimuthal angles of vector $\boldsymbol{r}_{ij}$ in a given reference frame. The term "bond" refers to the unit vector $\boldsymbol{r}_{ij}$ joining a reference atom i to any neighboring atom j within a cutoff radius r_{cut}. The cutoff radius is generally taken to be 1.2 times the first minimum in a radial distribution function (RDF). The local order around any atom i is an average over all its bonds with the neighboring N_{nb} atoms and is given by

$$q_{lm}(i) = \frac{1}{N_{nb}(i)} \sum_{j=1}^{N_{nb}(i)} Y_{lm}(r_{ij}). \tag{4.4}$$

An average of q_{lm} over all N atoms in a cluster gives the global bond order parameter:

$$Q_l = \left(\frac{4\pi}{2l+1} \sum_{m=-l}^{l} |\bar{Q}_{lm}|^2 \right)^{1/2}, \tag{4.5}$$

TABLE II. Bond order parameter for various geometries.

Geometry	Q_4	Q_6
FCC	0.19094	0.57452
HCP	0.09722	0.48476
BCC	0.03637	0.51069
Icosahedral	0	0.66332
Liquid/amorphous	0	0

where

$$\bar{Q}_{lm} = \frac{\sum_{i=1}^{N} N_{nb} q_{lm}(i)}{\sum_{i=1}^{N} N_{nb}(i)} \qquad (4.6)$$

The value of the global bond order parameter Q_l in a solid cluster depends on the relative bond orientations and has a unique value for each crystal structure. Based on local solid symmetry, it was found that cubic and decahedral clusters have nonzero values of $Q_l(i)$ for $l \geqslant 4$ and at $l = 6$ for those with icosahedral symmetry. All global order parameters vanish in isotropic liquids for $l > 0$. The global bond order values for different types of symmetry are reported in Table II. The atoms in a solid undergo vibrations about their equilibrium positions, leading to distortion of the crystal structure, which is characterized by Q_4 and Q_6 values.

The thermal evolution of the bond orientational order parameters for the various alloy compositions and for each of the three annealing cycles is shown in Fig. 6. The initial Q_6 parameter at 300 K for the nanoclusters during the first annealing cycle corresponds to ∼0.663, which is indicative of our icosahedral starting configuration. As the temperature is increased, we find that the order parameter shows a decrease owing to the onset of disorder in the crystalline structure. In crystalline solids, bond orientational order correlations persist over large distances, leading to order parameters with finite values. In the liquid phase, on the other hand, such correlations decay quickly with growing distance and the bond order parameters vanish. The melting point can be estimated from the variations in the bond order parameter values, as shown in Fig. 6. At the melting transition, all the order parameters (Fig. 6) change rapidly to zero, indicating a transition to isotropic liquid phase. We observe from Fig. 6 that the order parameters have finite values for temperatures <800 K before undergoing a sudden decrease to near zero-values. The temperature at which this structural transition from crystalline to liquid occurs depends on the alloy composition. For increasing Ag composition, during the first annealing cycle, we observe that this transition temperature changes from ∼1100 K for 50%Cu-50%Ni to ∼810 K for 50%Ag-25%Cu-25%Ni. This is consistent with the calculated melting points obtained based on variation in thermodynamics properties.

Upon cooling down to room temperatures ∼300 K, we observe differing structural features which are dependent on the ternary alloy composition. For Ag compositions of less than 20%, we observe that the annealed structure at 300 K has a finite Q_6 order parameter ∼0.3 whereas for Ag compositions higher than 20%, the annealed ternary alloy nanostructure at 300 K can be characterized as amorphous. For Ag compositions less than 20% in the ternary alloy, the
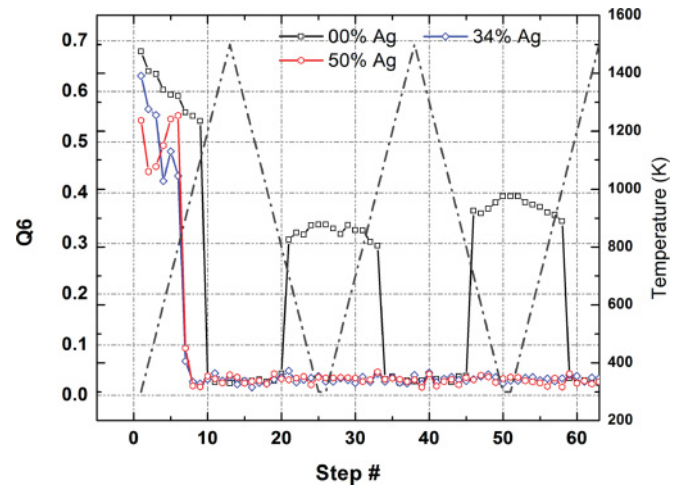

FIG. 6. (Color online) Evolution of bond orientational order parameter (Q_6) as a function of the simulation temperature for the various Ag-Cu-Ni ternary alloy nanocluster compositions. The dash-doted line gives variation of temperature as function of the simulation step and shows the sequence of heating-cooling cycles. The corresponding Q_6 order parameters for the various alloy compositions are represented by different markers.

freezing transition occurs in the 700–750 K intervals with the exact transition temperature dependent on the composition of the ternary alloy.

The structural variation among the various ternary alloys is clearly evident during the second and third annealing cycles. It can be clearly seen that the binary 50%Cu-50%Ni alloy shows recrystallization to an ordered structure during both the second and third annealing cycles. The annealed structure 50%Cu-50%Ni is more representative of a cuboctahedron like structure, with Q_6 values closer to fcc values as shown in Fig. 7. Similar behavior is observed in the case of ternary alloys with low Ag compositions (⩽20%Ag). On the other hand, the addition of Ag to obtain compositions higher than 20%Ag in the Ag-Ni-Cu ternary alloy shows that the amorphous structure formed after the first annealing cycle is retained during the second and third cycles. The same is revealed in Fig. 8, where the initial icosahedral structure shows a transformation to a liquid phase at the melting point and recrystallizes to an amorphous phase. It should be noted that it is difficult to distinguish the freezing transition for this range of alloy composition (>20%Ag) based on structural parameters, although they can be predicted on the basis of thermodynamic properties. The thermal instability resulting from the addition of Ag to the Cu-Ni alloy thus manifests itself in the form of a structural transformation from a crystalline to amorphous phase. It appears that this structural transformation and the onset of thermal instability is more pronounced for Ag compositions approaching 20% and higher in the Ag-Cu-Ni ternary alloy. The role of thermal annealing toward inducing a more homogeneous distribution of Ag across ternary alloy nanoclusters for higher Ag content and its effect on the mechanism of melting is discussed in the subsequent sections. The implication of the observed structural transformations and the resulting compositional variation on the thermal stability of the ternary alloys are also discussed in detail in a later section.
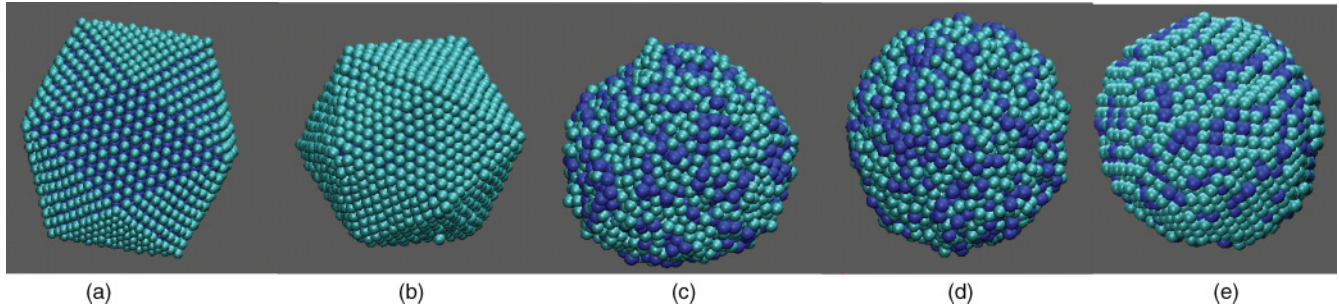
FIG. 7. (Color online) Snapshots showing the structural evolution of the 50%Cu-50%Ni nanocluster during the first annealing cycle. The snapshots shown correspond to (a) 300 K, (b) 600 K, (c) 1100 K (d) 700 K, (e) 300 K temperatures. The crystal structure transforms from an initial icosahedral structure in (a) to a liquid phase in (c) at the melting point. Upon cooling, the structure shown in (c) recrystallizes to the cuboctahedron shown in (e). Cu atoms are represented in light blue and Ni atoms are shown as dark blue spheres.

2. Radial distribution function

RDFs were used to investigate the structural disorder and the structural evolution of the thin films. The RDF is defined as the probability of finding an atom at a distance *r* from another atom compared with a homogeneous distribution and is given by[73–75]

$$g(r) = \frac{V}{N_1 N_2} \frac{1}{4\pi r^2 \delta r} \left\langle \sum_i \sum_{j>i} \delta(r - r_{ij}) \right\rangle.$$

In the above equation, V is the volume and N_1 and N_2 are the atom types of the RDF. The delta function in the RDF must give rise to a value of one for a range of r (δr), allowing for the formation of a fine histogram. The RDF would thus exhibit sharp peaks corresponding to a regular lattice structure and would tend to attain a value of 1 at longer distances. In the case of an amorphous system, the RDF shows characteristically smaller number of broad peaks at a short distance superimposed on an oscillatory trace to 1.0, indicating the loss of long-range order characteristic of amorphous systems.

Figure 9 shows the calculated RDFs for the various annealed binary and ternary alloy nanoclusters. The RDFs shown are calculated at the end of the third annealing cycle. It can be seen that the RDF for a Cu-Ni binary alloy shows sharp peaks corresponding to the near-neighbor distances. On the other hand, we observe from Fig. 9 that the RDFs for the 34%Ag-33%Cu-33%Ni and 50%Ag-25%Cu-25%Ni ternary alloy nanoclusters show that the peaks are broader, which signifies a higher degree of structural disorder. The absence of long-range order in the calculated RDF for 34% and 50%Ag suggests that the addition of Ag to Cu-Ni alloy results in annealed structures which are amorphous in nature. This observation is consistent with the bond orientational order calculations discussed in the previous section.

To gain further insights into the structural differences between the Cu-Ni and Ag-Cu-Ni alloys, we computed various pair correlations for the alloys. Figure 10(a) shows the calculated pair distribution functions (PDFs) for Cu-Cu, Cu-Ni and Ni-Ni correlations in a 50%Cu-50%Ni binary alloy nanocluster. The solid lines represent the RDF for the initial icosahedral configuration which shows sharp peaks at distances corresponding to near-neighbor distances, indicat-

ing the presence of long-range crystalline order. When the nanocluster is heated beyond the melting point, the RDFs (not shown) showed broader peaks, which were indicative of the liquid phase. From the liquid phase, as the temperature is reduced sequentially to 300K to form the annealed structure, we find that the solid-like features begin to appear as is indicated by the distinct peaks [in the dashed line in Fig 10a] corresponding to near-neighbor distances in the lattice. Finally, the Cu-Cu, Cu-Ni, and Ni-Ni RDFs for the annealed Cu-Ni binary structure at 300 K indicate that the structure has fully recrystallized and resolved peaks are evident at distances as far as 7 Å, indicative of long-range order.

The RDFs for the various metal interactions shown in Figs. 10(b) and 10(c) for a 50%Ag-25%Cu-25%Ni ternary alloy nanocluster shows sharp peaks at distances corresponding to near-neighbor distances. The presence of long range order in the preannealed 50%Ag-25%Cu-25%Ni structures is indicative of a crystalline order. After annealing, the RDFs, represented by dashed lines for the various metal interactions in a 50%Ag-25%Cu-25%Ni ternary alloy nanocluster, show a characteristically smaller number of broad peaks. These indicate short-range order and loss of long-range orders, which is characteristic of amorphous systems. The calculated RDFs for annealed Ag-Cu-Ni ternary alloys with Ag compositions of <20% show sharp peaks which are indicative of crystalline order for lower Ag compositions. The RDF calculations thus confirm the observation that the addition of Ag to a Cu-Ni alloy to obtain Ag compositions of >20% results in onset of structural disorder upon thermal treatment. Further insights into the melting mechanism and role of Ag in inducing this structural transformation are discussed in the next section.

C. Mechanism of phase transition

To investigate the differences in the observed structural transitions and melting behavior with increasing Ag composition in the ternary alloy, we analyze compositional density profiles, self-diffusion coefficients, and mean-square displacements (MSDs). There is a strong correlation between the compositional distribution of alloy constituents, their diffusional characteristics, and the mechanism of melting and structural transition in ternary alloys. The details are discussed below.
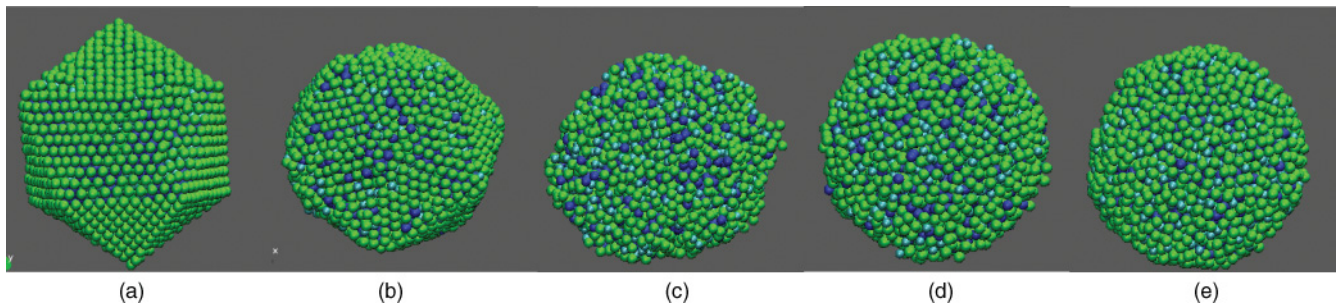
FIG. 8. (Color online) Snapshots showing the structural evolution of the 50%Ag-25%Cu-25%Ni nanocluster during the first annealing cycle. The snapshots shown correspond to (a) 300 K, (b) 600 K, (c) 1000 K, (d) 500 K, (e) 300 K temperatures. The crystal structure transforms from an initial icosahedral structure in (a) to a liquid phase in (c) at the melting point. Upon cooling, the structure shown in (c) recrystallizes to the amorphous structure shown in (e), which is retained during subsequent annealing cycles. Ag atoms are shown in green color, Cu atoms are represented in light blue and Ni atoms are shown as dark blue spheres.

1. Analysis of compositional density profiles

The composition variation across the nanocluster radius is represented in terms of the number density $\rho(r)$, which is defined as the number of atoms of a given type within a range of perpendicular positions in the simulation cell and normalized to the average density:[73–75]

$$\rho(r) = \frac{V}{NA\delta r} \left\langle \sum_i \delta(r - r_i) \right\rangle. \quad (4.7)$$

Here, V is the cluster volume, N is the number of atoms of a given type, A is the cluster area, and r_i is the distance of atom i from the cluster center. δr is typically the bin or histogram width and is the interval over which the ion densities are time averaged over many configurations obtained from the MD trajectories to compute the atomic number densities.

Figure 11 shows the atomic density distributions for the various constituent elements in a Cu-Ni and Ag-Cu-Ni alloys
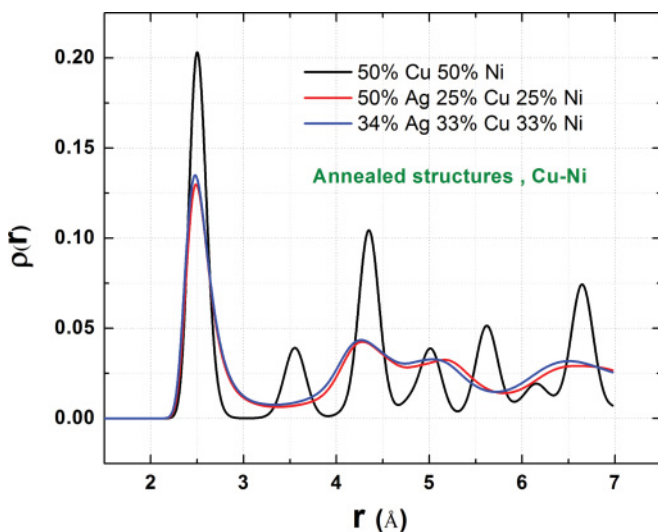

FIG. 9. (Color online) Calculated RDFs for the various annealed binary and ternary alloy nanoclusters. The RDF is calculated at the end of the third annealing cycle. The absence of long-range order in the calculated RDF for 34%Ag and 50%Ag suggests that the addition of Ag to Cu-Ni alloy results in annealed structures which are amorphous in nature.

before and after annealing. Figure 11(a) shows the Cu and Ni radial distributions obtained at the start of the first cycle (solid lines) and at the end of the third cycle (dashed lines). The initial compositional distribution represents a surface-segregated system where Cu atoms are located on the surface and the core is composed primarily of Ni [Fig. 11(a)]. At the end of the third annealing cycle, we find that Cu atoms migrate from the cluster surface to the interior. This is shown by the decrease in the peak located at the cluster surface, ~20 Å, and an increase in number densities at the cluster interior, ~10–15 Å. Simultaneously, there is also an outward migration of Ni atoms from the cluster interior to the surface, as can be seen by the increase in the peak located at ~17.5 Å and decrease in number densities for $r < 15$ Å. The annealing cycles thus lead to intermixing of the alloy constituents and a decrease in the initial segregation. This is corroborated by the snapshots shown in Fig. 7.

Figure 11(b) shows the compositional distribution for a 10%Ag-45%Cu-45%Ni ternary alloy. It can be seen that the preannealed structure comprises a surface-segregated system where primarily Ag atoms are located on the surface occupying the lowest coordination sites. The preannealed compositional profile in Fig. 11(b) therefore shows a peak at ~20–22 Å for Ag. The composition of Ag is not sufficient to cover all the surface sites, and hence we find that the remaining sites are occupied by Cu atoms as shown by the peak at ~20 Å whereas the core is composed primarily of Ni, as indicated by the higher number densities of Ni in comparison with Cu for $r < 20$ Å [Fig. 11(b)].

At the end of the third annealing cycle, we find that there is no appreciable change in the composition profile of the Ag for the 10%Ag-45%Cu-45%Ni ternary alloy. We also find that Cu atoms migrate from the cluster surface to the interior of the particle. This is shown by the decrease in the number densities located at ~15–20 Å and an increase in number densities at the cluster interior ~10–15 Å (regarding the preannealed configuration). This is accompanied by an outward migration of Ni atoms from the cluster interior to the surface, as can be seen by decrease in number densities for $r \sim 7.5$–15 Å and an increase in number densities for $r \sim 15$–20 Å. The annealing cycles for this ternary alloy composition lead to intermixing of the Cu and Ni constituents, while the Ag distribution is mostly unaffected. It is important to note that the heating-cooling rates
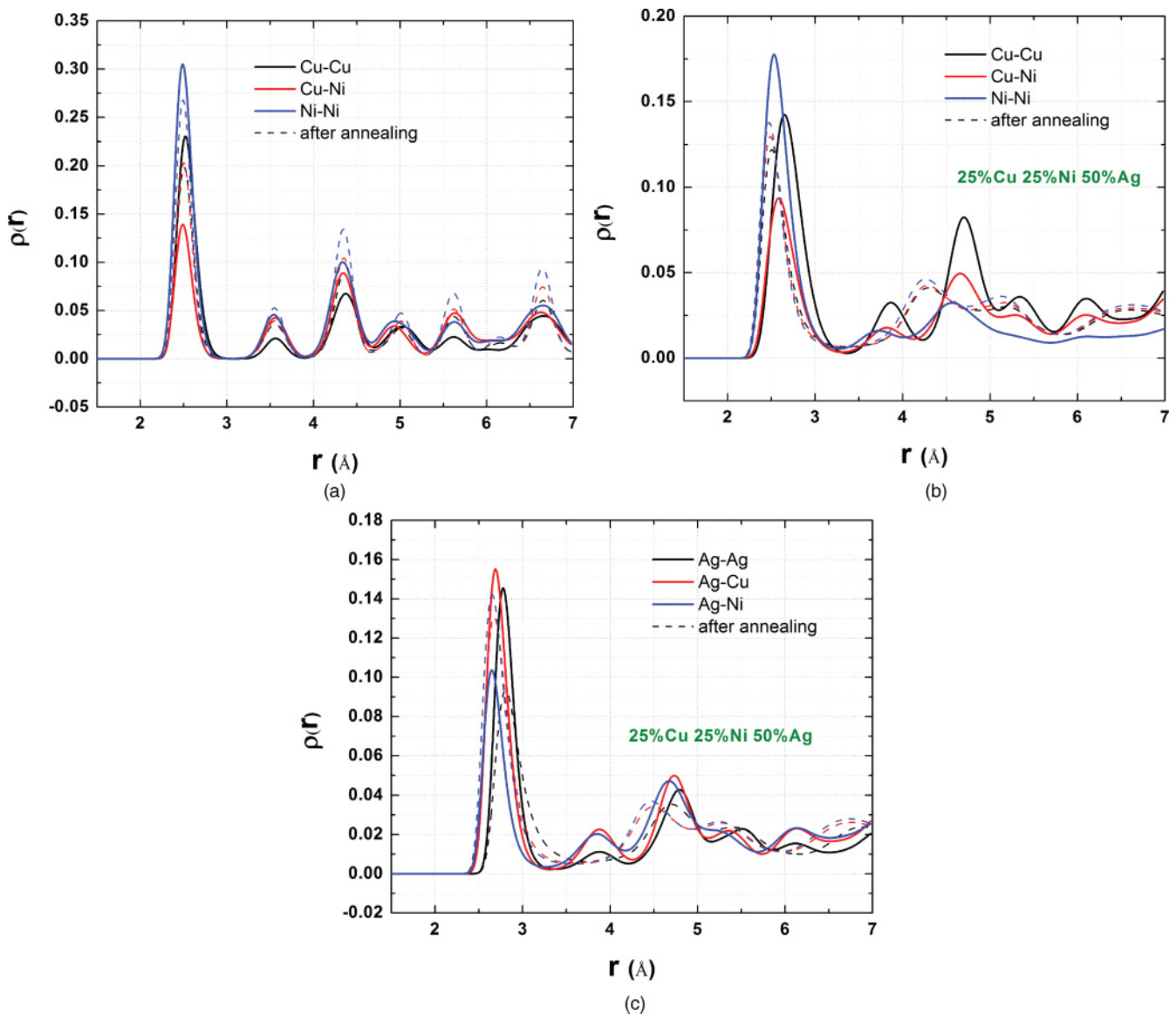
FIG. 10. (Color online) (a) Calculated PDFs for the various metal-metal interactions in a 50%Cu-50%Ni binary alloy nanocluster. The solid and dashed lines refer to PDFs obtained before and after the annealing cycles. The PDFs for the various metal interactions in a 50%Cu-50%Ni binary alloy nanocluster show sharp peaks at distances corresponding to near neighbor distances. The presence of long-order in the annealed Cu-Ni structures is indicative of a crystalline order being retained after the heating-cooling schedules. (b),(c) Calculated PDFs for the various metal-metal interactions in a 50%Ag-25%Cu-25%Ni ternary alloy nanocluster. (b) represents RDFs for Cu-Cu, Cu-Ni, and Ni-Ni correlations in the ternary alloy, whereas (c) represents Ag-Ag, Ag-Cu, and Ag-Ni correlations. The solid and dashed lines refer to PDFs obtained before and after the annealing cycles, respectively.

play a major role in determining the overall segregation profile after the annealing processs.

When the Ag composition in the ternary alloy nanocluster is further increased from 10% to 20% to form the 20% Ag-30%Cu-30%Ni alloy, we observe that the annealing cycles result in intermixing of Ag in addition to Cu and Ni. Figure 11(c) shows the decrease in number densities of Ag on the outer surface, i.e., for $r \sim 17.5$–25 Å, whereas the number densities of Ag in the cluster interior increase, i.e., for $r \sim 5$–17.5 Å. This indicates that Ag migrates from the surface to the interior. It is important to point out that for Ag compositions of <20% the number of Ag atoms is not sufficient to completely make up the surface of the alloy

nanoparticle. During the annealing cycles, we find that the coordinates or positions occupied by Ag atoms (originally that of the vertices and edges) are still populated by Ag atoms. The surface atoms of Ag show a higher proclivity to migrate to the core of the particle compared with the vertices and edges. The effect of annealing on Cu and Ni distributions for this ternary alloy composition is similar to that observed for 50%Cu-50%Ni and 10%Ag-45%Cu-45%Ni alloys. We observe a similar effect of annealing on Ag, Cu, and Ni distributions for a higher composition of Ag in the ternary alloy nanocluster. The 20% Ag composition thus appears to represent a threshold above which we begin to observe Ag migration from the surface to the interior. Below this
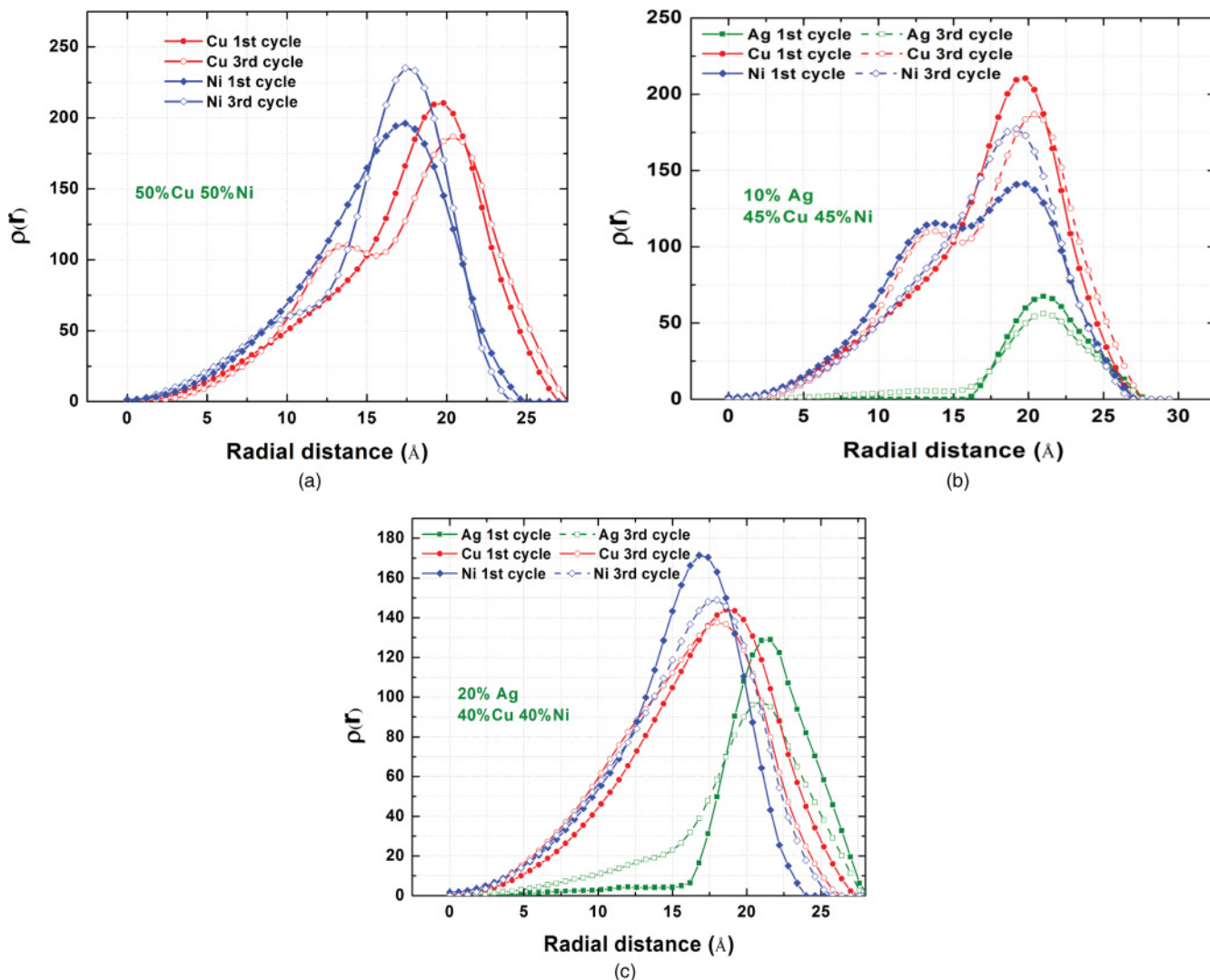
FIG. 11. (Color online) Compositional variations across the nanocluster radius for 50%Cu-50%Ni, 10%Ag-45%Cu-45%Ni, and 20%Ag-30%Cu-30%Ni alloys. The solid and dashed lines represent compositions before and after annealing, respectively.

Ag composition [Figs. 11(a)–11(c)], the initial segregation profile of Ag is unaffected by the annealing cycle. The observed difference in the Ag compositional distributions for the ternary alloys upon annealing thus has an interesting effect on their thermal stability and melting characteristics. It should be noted that 20% Ag composition represents the ternary alloy composition above which annealing resulted in decrease in melting point. We further investigate the implications of this annealing-induced Ag composition redistribution on the melting mechanism of the ternary alloys.

2. Analysis of surface melting characteristics

(a) Calculation of self diffusion coefficients. The self-diffusion coefficients can be obtained from either the positions or velocities of molecules. The MSD is proportional to the observation time in the limit as time tends to infinity. The

proportionality constant relating the MSD to observation time is known as self-diffusivity D, which is given by

$$D \equiv \frac{1}{2d} \lim_{t \to \infty} \frac{\langle [r(t_0 + t) - r(t_0)]^2 \rangle}{t}, \quad (4.8)$$

where d is the dimensionality of the system and $r(t)$ refers to the vector position of molecule at time t. The ensemble average is taken over all molecules in the system and over several time origins.

Figure 12(a) shows the diffusion coefficients calculated at various temperatures for the various ternary alloy compositions before and after the annealing cycles. At the melting point, the atomic diffusivities show a sharp increase, indicating a first-order transition from the solid to liquid phase. In the liquid phase, the diffusion coefficients show a tendency to increase rapidly with temperature. We observe that the preannealed structure having 50%Cu-50%Ni begins to surface melt at ∼900 K whereas the annealed structure shows delayed surface-melting onset, ∼1000 K. On the other hand, the preannealed
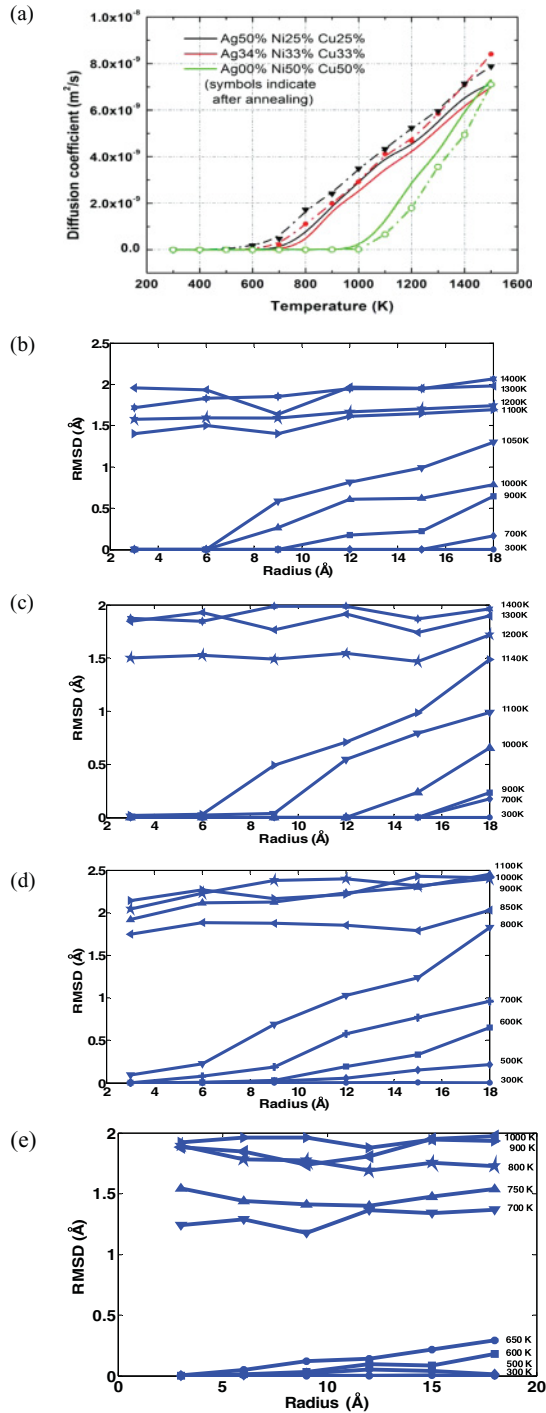
FIG. 12. (Color online) (a) Variations of the self-diffusion coefficient with temperature for the various compositions of the ternary alloys. Ag composition is increased from 0 to 50%. Solid lines indicate diffusion coefficients at various temperatures before annealing whereas dashed lines with markers are used to indicate the diffusion coefficients after annealing. (b)–(e) Root MSD calculated for atoms in various shells for 50%Cu-50%Ni and 50%Ag-25%Cu-25%Ni as a function of distance from the center of cluster. (b) and (c) represent the shell-based root MSD calculated for preannealed and annealed configurations, respectively, for the 50%Cu-50%Ni alloy. (d) and (e) represent the shell-based root MSD calculated for preannealed and annealed configurations, respectively, for the 50%Ag-25%Cu-25%Ni ternary alloy.

34%Ag ternary alloy begins to surface melt at ∼700 K, which decreased to ∼600 K upon annealing. Similarly, the preannealed 50%Ag ternary alloy surface melts at ∼650 K, which decreases to ∼500 K upon annealing.

(b) Surface melting and the Lindemann criterion. Further insight into the exact melting mechanism can be obtained by partitioning the cluster into radial shells of equal width *dR*. Root-mean-square displacement (RMSD) calculated within each shell was calculated for atoms in that shell:

$$\text{RMSD}_{\text{shell}}(dt) = \frac{\sum_{i \in \text{shell}} \text{RMSD}_i(dt)}{N_{\text{shell}}}, \qquad (4.9)$$

where

$$\text{RMSD}(dt) = \sqrt{\left\langle \sum_{t=0}^{T-dt} (r_i(t+dt) - r_i(t))^2 \right\rangle}. \quad (4.10)$$

The average interatomic distance (∼3 Å) between atoms was used as *dR*. The atoms were assigned to the bins based on their initial positions at the end of the equilibration period. The MSDs for each shell were then generated by averaging over a 200–500-ps trajectory with sampling done every 0.1 ps. For lower temperatures the averaging was done over a larger trajectory (>1 ns) to account for low atomic jump frequencies. At higher temperatures, averages taken over a 200–500-ps trajectory with different origins gave the same result, which is indicative of a system that is truly in equilibrium.

The RMSD was assigned to each shell, and its dependence on distance from the center of cluster was carried out [Figs. 12(b)–12(e)]. In the case of a Cu-Ni binary alloy having 50%Cu, we find the RMSD of outer shells in both the preannealed and postannealed configurations to be higher than for core atoms owing to the surface atoms having higher degrees of freedom for surface atoms. Similar behavior is observed for the preannealed 50%Ag-25%Cu-25%Ni ternary alloy. At the melting point, the RMSD changes dramatically, indicative of first-order transition. One can define a critical RMSD value for the atoms above which the atoms can be considered to have undergone a melting transition. The Lindemann criterion predicts the melting transition to occur when atomic motion exceeds 10%–15% of the interatomic distance (∼3 Å in our case). For the calculated trajectories shown in Figs. 12(b)–12(e), the critical RMSD can be taken as ∼0.60 Å, which corresponds to ∼20% of the average interatomic distance. The atomic shells exceeding this diffusivity value can be considered as having undergone the solid-liquid phase transition.

In the case of a preannealed configuration having 50%Cu-50%Ni, shown in Fig. 12(b), the shells exhibit solid-like behavior for temperatures below 1000 K. At 1000 K, we observe that the atoms corresponding to approximately three shells have become molten whereas the innermost core shell still maintains solid-like features. On the other hand, the calculated shell-based RMSD for the annealed structure having 50%Cu-50%Ni at 1000 K [Fig. 12(c)] suggests that only the outermost shell have melted whereas the three innermost shells still remain a crystalline solid. Therefore, on a volume basis,

we find that at 1000 K almost 75%–80% of the preannealed 50%Cu-50%Ni structure has melted whereas only 20%–25% of the annealed structure at 1000 K has transitioned into the liquid phase. Annealing in the case of 50%Cu-50%Ni thus results in suppression of surface-melting characteristics and improves the thermal stability of the binary alloy Cu-Ni nanocluster.

The effect of Ag addition on the surface-melting characteristics of the ternary alloy nanocluster is shown in Figs. 12(d) and 12(e). We find the onset of surface-melting characteristics as early as 600 K for the 50%Ag-25%Cu-25%Ni alloy, indicative of enhanced surface melting at higher Ag compositions, arising from the presence of Ag atoms on the surface. Comparison of the preannealed and postannealed configurations for the ternary alloy with 50%Ag shows that while the preannealed configuration exhibits surface-melting characteristics, the annealed configuration shows significantly reduced surface-melting features. In the case of the pre-annealed configuration, we observe that the two outermost shells at 700 K have transformed from solid to liquid. As the temperature increases to 800 K, the four outermost shells exhibit liquid-like features, and at higher temperatures, we observe that the cluster has completely melted. On the other hand, in the case of the annealed configuration, we observe that in the 300–650 K range, the RMSD values of all the shells do not exceed the critical diffusivity values. Note that the RMSD of the outermost shell at 600–650 K is only slightly higher than the rest. As the temperature increases from 650 to 700 K, the RMSD values of all the shells increase significantly and approach 1.2–2 Å, which is much higher than the critical RMSD value of 0.6 Å. The cluster has almost entirely undergone the melting transition and resembles a more homogeneous melting. Hence, the effect of annealing on ternary alloys with 50%Ag is to significantly suppress the surface-melting characteristics and reduce the thermal stability of the nanocluster. Our calculations of shell-based RMSDs at other Ag compositions in the ternary alloy suggests that the onset of surface melting is strongly dependent on Ag composition; higher Ag compositions lead to decreased surface melting and an earlier onset of the melting transition for postannealed configurations.

The role of thermal annealing cycles toward inducing a more homogeneous distribution of Ag across ternary alloy nanoclusters for higher Ag content and its effect on the mechanism of melting can be discussed further based on the calculated RMSD for each of the alloy constituents. In particular, the transport of Ag atoms across the nanocluster can lead to a change in the mechanism of melting. It is known that the melting points of the components vary as Ag < Cu < Ni for the pure components. The cluster structure initially is surface segregated, and Ag atoms with lower surface energy are located on the surface occupying low coordinated sites. This allows for a heterogeneous melting mechanism wherein the nanocluster melting is typically initiated at the surface. The melting then proceeds to the core, and the overall cluster melting point is dictated by the melting characteristics of the core atoms, i.e., Cu and Ni. If this surface-segregation profile is preserved or enhanced during subsequent annealing cycles, then the surface-melting characteristics or the heterogeneous melting mechanism ensures that the cluster melting point is

dictated by the melting characteristics of the core components. This is especially true in the case of Ag compositions of less than 20% in the ternary alloy, where Ag remains segregated even after three annealing cycles.

On the other hand, if the annealing cycles were to completely disrupt the initial segregation profile and result in a homogeneous distribution of the Ag across the nanocluster, then one can observe a more bulklike melting characteristic where the cluster melting characteristics are essentially dictated by the low melting Ag component distributed through the bulk of the nanocluster. For compositions above 20%Ag in the ternary alloys, our analysis of the compositional profiles indicates a more homogeneous Ag distribution. For such a distribution, the melting mechanism shifts from a surface-initiated melting to a more homogeneous melting behavior. The overall melting point of the nanocluster is thus dictated by the melting behavior of the Ag component, and therefore we observed a significant drop in the melting point after the first annealing cycle for higher Ag content (>20%). This explains the annealing-induced thermal instability for higher Ag content in the ternary alloy. This paper clearly brings out the role of compositional distribution in controlling the thermal characteristics of ternary alloys.

V. CONCLUSIONS

MD simulations have been used to investigate the melting behavior of Ag-Cu-Ni ternary alloy nanoclusters of 4-nm diameter and varying compositions. The melting characteristics were studied for a series of three annealing cycles. The melting points calculated based on thermodynamic properties indicate that the addition of Ag results in a decrease in melting point during the first annealing cycle. The melting behavior during subsequent annealing cycles differs for the ternary alloy and is found to depend on the Ag composition. While Cu-Ni alloys show a monotonic increase in melting point upon annealing, the Ag-Cu-Ni alloys show a nonmonotonic variation in melting point. For Ag compositions below 20%, we observe an initial increase in melting point followed by a slight decrease. On thermal annealing, Ag-rich ternary alloys show a rapid decrease in melting point with rates proportional to the Ag content. The structural transformation associated with this melting transition was characterized by bond orientational order parameters. We observe a structural transformation from an icosahedral to a cuboctahedron for a Cu-Ni alloy having 50%Cu. The Ag addition beyond 20% results in transformation into an amorphous structure during the first annealing cycle which is retained during subsequent annealing runs. The analysis of RDFs for the various pairs confirms this structural transformation.

Shell-based RMSDs offer better insight into the mechanism of the melting transition. We find that the melting of Cu-Ni binary alloys is characterized by a heterogeneous melting mechanism which involves premelting of the surface-segregated Cu atoms followed by melting of the Ni core. The addition of Ag to a Cu-Ni cluster results in transformation from an initial heterogeneous melting mechanism during the first annealing cycle to a bulk-like melting mechanism during

subsequent annealing runs. Compositional analyses based on radial atomic density profiles indicate that these transitions were dependent on the distribution of the alloying elements in the nanoclusters. The Ag in a ternary alloy migrates to the cluster core upon heating and becomes distributed through the cluster. Diffusion coefficients and RMSDs calculated based on the atomic trajectories indicate that the rate of mixing of Ag increases with Ag content in the Ag-Cu-Ni ternary alloy. As a result, ternary alloys due to the homogeneous distribution of Ag after annealing cycles exhibit a bulk-like melting (or reduced surface-melting) behavior. The presence of low melting Ag in the cluster core for Ag-rich ternary alloys resulted in significant lowering of the melting temperature.

On the whole, the simulation results and the description of the melting transition agree qualitatively with available experimental studies on alloy nanoclusters.

*skrssank@anl.gov

[1] F. Tao, M. E. Grass, Y. Zhang, D. R. Butcher, J. R. Renzas, Z. Liu, J. Y. Chung, B. S. Mun, M. Salmeron, and G. A. Somorjai, Science **322**, 932 (2008).

[2] S. Sudhanshu, S. Aaron, C. Kevin, K. Ki-Sub, P. Paul, S. Kai, L. Jaebeom, X. Chuanlai, G. D. Lilly, S. C. Glotzer, and N. A. Kotov, Science **327**, 1355 (2010).

[3] M. Pelton, J. E. Sader, J. Burgin, M. Liu, P. Guyot-Sionnest, and D. Gosztola, Nat. Nanotechnol. **4**, 492 (2009).

[4] D. Alloyeau, C. Ricolleau, C. Mottet, T. Oikawa, C. Langlois, L. Bouar, N. Braidy, and A. Loiseau, Nat. Mater. **8**, 940 (2009).

[5] W.-H. Chiang and R. M. Sankaran, Nat. Mater. **8**, 882 (2009).

[6] V. R. M. Stamenkovic, B. Simon, M. Arenz, K. J. J. Mayrhofer, C. A. Lucas, G. Wang, P. N. Ross, and N. M. Markovic, Nat. Mater. **6**, 241 (2007).

[7] L.-L. Wang and D. D. Johnson, J. Am. Chem. Soc. **131**, 14023 (2009).

[8] E. V. Shevchenko, D. V. Talapin, N. A. Kotov, S. O'Brien, and C. B. Murray, Nature (London) **439**, 55 (2006).

[9] J. Luo, L. Han, N. N. Kariuki, L. Wang, D. Mott, C.-J. Zhong, and T. He, Chem. Mater. **17**, 5282 (2005).

[10] Y.-G. Guo, J.-S. Hu, and L.-J. Wan, Adv. Mater. **20**, 4384 (2008).

[11] Y. C. Lu, Z.C. Xu, H. A. Gasteiger, S. Chen, K. Hamad-Schifferli, and Y. Shao-Horn, J. Am. Chem. Soc. **35**, 12170 (2010).

[12] S. Chen, P. J. Ferreira, W. C. Sheng, N. Yabuuchi, L. F. Allard, and Y. Shao-Horn, J. Am. Chem. Soc. **130**, 13818 (2008).

[13] R. Ferrando, J. Jellinek, and R. L. Johnston, Chem. Rev. **108**, 845 (2008).

[14] J. Luo, L. Wang, D. Mott, P. N. Njoki, N. Kariuki, C.-J. Zhong, and T. He, J. Mater. Chem. **16**, 1665 (2006).

[15] Y. Zhang, Y. H. Wen, Z. Z. Zhu, and S. G. Sun, J. Phys. Chem. C **114**, 18841 (2010).

[16] A. Hu, J. Y. Guo, H. Alarifi, G. Patane, Y. Zhou, G. Compagnini, and C. X. Xu, Appl. Phys. Lett. **97**, 153117 (2010).

[17] A. Aguado and M. F. Jarrold, Annu. Rev. Phys. Chem. **62**, 151 (2011).

[18] S. K. R. S. Sankaranarayanan, V. R. Bhethanabotla, and B. Joseph, Phys. Rev. B **71**, 195415 (2005).

[19] A. A. Dzhurakhalov and M. Hou, Phys. Rev. B **76**, 045429 (2007).

[20] H. Jiang, K. S. Moon, and C. P. Wong, in *Proceedings of the International Symposium on Advanced Packaging Materials: Processes, Properties and Interfaces* (2005), pp. 173–77 (IEEE Library).

[21] S. Piccinin, S. Zafeiratos, C. Stampfl, T. W. Hansen, M. Hävecker, D. Teschner, V. I. Bukhtiyarov, F. Girgsdies, A. Knop-Gericke, R. Schlogl, and M. Scheffler, Phys. Rev. Lett. **104**, 035503 (2010).

[22] S. Chowdhury, V. R. Bhethanabotla, and R. Sen, J. Phys. Chem. C **113**, 13016 (2009).

[23] T. Yamauchi, Y. Tsukahara, T. Sakata, H. Mori, T. Yanagida, T. Kawai, and Y. Wada, Nanoscale **2,** 515 (2010).

[24] Z. Zhang, T. M. Nenoff, K. Leung, S. R. Ferreira, J. Y. Huang, D. T. Berry, P. P. Provencio, and R. Stumpf, J. Phys. Chem. C **114**, 14309 (2010).

[25] W. H. Qi and S. T. Lee, J. Phys. Chem. C **114**, 9580 (2010).

[26] F. Chen, B. C. Curley, G. Rossi, and R. L. Johnston, J. Phys. Chem. C **111**, 9157 (2007).

[27] S. K. R. S. Sankaranarayanan, V. R. Bhethanabotla, and B. Joseph, J. Phys. Chem. C **111**, 2430 (2007).

[28] S. K. R. S. Sankaranarayanan, V. R. Bhethanabotla, and B. Joseph, Phys. Rev. B **76**, 134117 (2007).

[29] S. K. R. S. Sankaranarayanan, V. R. Bhethanabotla, and B. Joseph, Phys. Rev. B **72**, 195405 (2005).

[30] S. K. R. S. Sankaranarayanan, V. R. Bhethanabotla, and B. Joseph, Phys. Rev. B **74**, 155441 (2006).

[31] Y. Qi, T. Çagin, and W. L. Johnson, and W. A. Goddard, III, J. Chem. Phys. **115**, 385 (2001).

[32] L. J. Lewis, P. Jensen, and J.-L. Barrat, Phys. Rev. B **56**, 2248 (1997).

[33] S.-P. Huang and P. B. Balbuena, J. Phys. Chem. B **106**, 7225 (2003).

[34] J. H. Sinfelt, *Bimetallic Catalysts—Discoveries, Concepts, and Applications* (Wiley, New York, 1983).

[35] Z. Kuntová, G. Rossi, and R. Ferrando, Phys. Rev. B **77**, 205431 (2008).

[36] O. A. Oviedo, M. M. Mariscal, and E. P. M. Leiva, Phys. Chem. Chem. Phys. **12**, 4580 (2010).

[37] S. Xiao, W. Hu, W. Luo, Y. Wu, X. Li, and H. Deng, Eur. Phys. J. B Cond. Matt. Complex Syst. **54**, 479 (2006).

[38] S. J. Mejía-Rosales, C. Fernández-Navarro, and E. Pérez-Tijerina, J. Phys. Chem. B **110**, 12884 (2006).

[39] A. Aguado and J. M. López, J. Chem. Theory Comput. **1**, 299 (2005).

[40] I. Parsina and F. Baletto, J. Phys. Chem. C **114**, 1504 (2010).

[41] Z. Yang, X. Yang, Z. Xu, and S. Liu, Phys. Chem. Chem. Phys. **11**, 6249 (2009).

[42] Y. Sun and Y. Xia, Science **298**, 2176 (2002).

[43] N. R. Jana, L. Gearheart, and C. J. Murphy, Adv. Mater. **13**, 1389 (2001).

[44] G. Wang, M. A. Van Hove, P. N. Ross, and M. I. Baskes, Prog. Surf. Sci. **79**, 28 (2005).

[45] G. Wang, M. A. Van Hove, P. N. Ross, and M. I. Baskes, J. Chem. Phys. **122**, 024706 (2005).

[46] G. Wang, M. A. Van Hove, P. N. Ross, and M. I. Baskes, J. Chem. Phys. **121**, 5410 (2004).

[47] H. N. G. Wadley, X. Zhou, R. A. Johnson, and M. Neurock, Prog. Mater. Sci. **46**, 329 (2001).

[48] R. A. Johnson, Phys. Rev. B **39**, 12554 (1989).

[49] L. Q. Yang and A. E. Depristo, J. Catal. **148**, 575 (1994).

[50] L. Zhu and A. E. DePristo, J. Catal. **167**, 400 (1997).

[51] L. Zhu and A. E. DePristo, J. Chem. Phys. **102**, 5342 (1995).

[52] M. Gaudry, E. Cottancin, M. Pellarin, J. Lerme, L. Arnaud, J. R. Huntzinger, J. L. Vialle, and M. Broyer, Phys. Rev. B **67**, 155409 (2003).

[53] F. F. Abraham and C. R. Bundle, Acta Mater. **55**, 1617 (2007).

[54] F. F. Abraham and C. R. Brundle, J. Vac. Sci. Technol. **18**, 506 (1981).

[55] K. Wandelt and C. R. Brundle, Phys. Rev. Lett. **46**, 1529 (1981).

[56] M. Polak and L. Rubinovich, Surf. Sci. **584**, 41 (2005).

[57] L. Rubinovich and M. Polak, Phys. Rev. B **69**, 155405 (2004).

[58] W. Smith and T. R. Forester, J. Mol. Graphics **14**, 136 (1996).

[59] Y. Kimura, Y. Qi, T. Cagin, and W. A. Goddard III, in *MRS Symposia Proceedings* (Materials Research Society, Pittsburgh, PA, 1999), No. 554, p. 43.

[60] A. P. Sutton and J. Chen, Philos. Mag. Lett. **61**, 139 (1990).

[61] C. J. Smithells, E. A. Brandes, and G. B. Brook, *Smithells Metals Reference Book* (Butterworth-Heinemann, Oxford, Boston, 1992).

[62] R. R. Hultgren, R. R. Hultgren, and American Society for Metals, *Selected Values of the Thermodynamic Properties of the Elements* (American Society for Metals, Metals Park, OH, 1973).

[63] Y. Teng, X. Zeng, and D. Sun, J. Phys. Chem. B **111**, 2309 (2007).

[64] L.S. Pan, H. P. Lee, and C. Lu, Eur. Phys. J. D Atom. Molec. Opt. Plasma Phys. **50**, 27 (2008).

[65] Z.-A. Tian, R.-S. Liu, C.-X. Zheng, H.-R. Liu, Z.-Y. Hou, and P. Peng, J. Phys. Chem. A **112**, 12326 (2008).

[66] J. Davoodi and M. Ahmadi, Diffusion and Defect Data Solid State Data, Pt. A Defect and Diffusion Forum **297–301** (Pt. 1, Diffusion in Solids and Liquids V), 543 (2010).

[67] H. Reiss, P. Mirabel, and R. L. Whetten, J. Phys. Chem. **92**, 7241 (1988).

[68] R. Kofman, P. Cheyssac, A. Aouaj, Y. Lereah, G. Deutscher, T. Ben-David, J. M. Penisson, and A. Bourret, Surf. Sci. **303**, 231 (1994).

[69] M. Schmidt, R. Kusche, W. Kronmuller, B. von Issendorff, and H. Haberland, Phys. Rev. Letts. **79**, 99 (1997).

[70] Y. G. Chushak and L. S. Bartell, J. Phys. Chem. B **107**, 3747 (2003).

[71] T. Morishita, J. Chem. Phys. **113**, 2976 (2000).

[72] P. J. Steinhardt, D. R. Nelson, and M. Ronchetti, Phys. Rev. B **28**, 784 (1983).

[73] M. P. Allen and D. J. Tildesley, *Computer Simulation of Liquids* (Oxford University Press, Oxford, 1989).

[74] D. Frenkel and B. Smit, *Understanding Molecular Simulation: From Algorithms to Applications* (Academic, San Diego, 2002).

[75] J. M. Haile, *Molecular Dynamics Simulation: Elementary Methods* (Wiley, New York, 2001).